



OPEN ACCESS

EDITED BY

Qitong Huang,
Gannan Medical University, China

REVIEWED BY

Zhijin Fan,
Sun Yat-sen University, China
Ming Hu,
Nanjing Tech University, China

*CORRESPONDENCE

Zhijun Zhang,
✉ zjzhang@zstu.edu.cn
Guixian Hu,
✉ hugx_shiny@163.com

†These authors have contributed equally to this work

RECEIVED 13 December 2023

ACCEPTED 03 January 2024

PUBLISHED 16 January 2024

CITATION

Li X, Zhu W, Zhou Y, Wang N, Gao X, Sun S, Cao M, Zhang Z and Hu G (2024), Near-infrared light-heatable platinum nanozyme for synergistic bacterial inhibition. *Front. Bioeng. Biotechnol.* 12:1355004. doi: 10.3389/fbioe.2024.1355004

COPYRIGHT

© 2024 Li, Zhu, Zhou, Wang, Gao, Sun, Cao, Zhang and Hu. This is an open-access article distributed under the terms of the [Creative Commons Attribution License \(CC BY\)](https://creativecommons.org/licenses/by/4.0/). The use, distribution or reproduction in other forums is permitted, provided the original author(s) and the copyright owner(s) are credited and that the original publication in this journal is cited, in accordance with accepted academic practice. No use, distribution or reproduction is permitted which does not comply with these terms.

Near-infrared light-heatable platinum nanozyme for synergistic bacterial inhibition

Xue Li^{1,2†}, Weisheng Zhu^{3†}, Yuan Zhou^{4,5}, Nan Wang³, Xiangfan Gao³, Suling Sun¹, Mengting Cao³, Zhijun Zhang^{3,6*} and Guixian Hu^{1*}

¹Institute of Agro-product Safety and Nutrition, Zhejiang Academy of Agricultural Sciences, Hangzhou, China, ²Key Laboratory of Information Traceability for Agricultural Products, Ministry of Agriculture and Rural Affairs of China, Hangzhou, Zhejiang, China, ³Key Laboratory of Surface & Interface Science of Polymer Materials of Zhejiang Province, School of Chemistry and Chemical Engineering, Zhejiang Sci-Tech University, Hangzhou, China, ⁴Department of Pharmacy, Taihe Hospital, Hubei University of Medicine, Shiyan, China, ⁵College of Pharmacy, Hubei University of Traditional Chinese Medicine, Wuhan, China, ⁶Shengzhou Innovation Research Institute of Zhejiang Sci-Tech University, Shengzhou, China

The development of non-antibiotic strategies for bacterial disinfection is of great clinical importance. Among recently developed different antimicrobial strategies, nanomaterial-mediated approaches, especially the photothermal way and reactive oxygen species (ROS)-generating method, show many significant advantages. Although promising, the clinical application of nanomaterials is still limited, owing to the potential biosafety issues. Further improvement of the antimicrobial activity to reduce the usage, and thus reduce the potential risk, is an important way to increase the clinical applicability of antibacterial nanomaterials. In this paper, an antimicrobial nanostructure with both an excellent photothermal effect and peroxidase-like activity was constructed to achieve efficient synergistic antimicrobial activity. The obtained nano-antimicrobial agent (ZIF-8@PDA@Pt) can not only efficiently catalyze the production of ROS from H₂O₂ to cause damage to bacteria but also convert the photon energy of near-infrared light into thermal energy to kill bacteria, and the two synergistic effects induced in a highly efficient antimicrobial activity. This study not only offers a new nanomaterial with efficient antibacterial activity but also proposes a new idea for constructing synergistic antibacterial properties.

KEYWORDS

nanozyme, metal–organic framework, photothermal effect, reactive oxygen species, bacterial inhibition

1 Introduction

Bacterial infection is a serious threat to global health, which is estimated to be the second leading cause of death worldwide, accounting for one in eight of all deaths in 2019 (Ikuta et al., 2022). Antibiotics, also known as antimicrobials, are the most commonly used treatment for bacterial infections. Antibiotics are a class of secondary metabolites produced by microorganisms or higher plants and animals, which have shown high activity against bacterial infections. However, bacteria develop resistance to antibiotics over time, and the problem of bacterial resistance is growing due to the misuse of antibiotics. It is estimated that more than 1.2 million people—and potentially millions more—died globally a year as a direct result of antibiotic-

resistant bacterial infections, according to the most comprehensive estimate, to date, of the AMR (Murray et al., 2022). Unfortunately, the rate of development of new antibiotics is much slower than the rate of emergence of bacterial resistance. In addition, the use of antibiotics for anti-infective therapy is prone to side effects such as liver damage and kidney injury. Thus, the development of novel antimicrobial strategies to reduce the use of antibiotics is of great clinical importance.

Many different new antimicrobial strategies have been reported in recent years (Sun et al., 2020; Niu et al., 2021a; Niu et al., 2021b; Du et al., 2021; Zhang et al., 2021; Li et al., 2022a; Li et al., 2022b; Fu et al., 2022; Guo et al., 2022; Wang et al., 2023; Wu et al., 2023). Among them, nanomaterial-mediated antimicrobial strategies show more significant advantages, including easy material synthesis, being less susceptible to bacterial resistance, and a high bacterial killing efficiency. In these strategies, nanomaterials usually play the role of mediators of energy or material conversion. Typically, nanomaterials can convert the energy of external physical stimuli into thermal energy that can directly damage the bacterial structure (Liu et al., 2022a; Hu et al., 2022). The photothermal antimicrobial strategy is such an energy conversion-based bacterial disinfection method, which is favored for its high killing efficiency and spatial and temporal controllability (Han et al., 2020). The photothermal effect is a property of materials that can harvest and transfer the photon energy from irradiated light to heat energy, which is promising for wide applications (Wang et al., 2019; Wu and Yeow, 2022; Zeng et al., 2022; Fan et al., 2023; Huang et al., 2023; Jiao et al., 2023; Yue et al., 2023; Zhao et al., 2023; Zhu et al., 2023). In the photothermal antimicrobial strategy, nanomaterials with photothermal conversion efficiency, such as graphene, Fe₃O₄, polydopamine (PDA), and gold nanostructures, can efficiently convert the photon energy of near-infrared light into thermal energy to achieve efficient killing of different types of bacteria (Niu et al., 2018; Wang et al., 2022). In addition, nanomaterials with enzyme-like activity can convert endogenous or exogenous chemicals into high-energy reactive oxygen species (ROS) to cause bacterial casualties (Chen et al., 2018; Liu et al., 2022b; Dorma Momo et al., 2022). For example, nanoenzymes such as graphene oxide and carbon dots can catalyze the production of ROS from highly expressed or exogenous H₂O₂ at the site of bacterial infection to cause the destruction of bacterial nucleic acids and proteins and thus lead to bacterial death. Nanomaterial-mediated antimicrobial strategies undoubtedly offer unlimited possibilities for replacing the use of antibiotics (Makabenta et al., 2021; Xie et al., 2023). Nevertheless, the clinical application of nanomaterials is still very limited at present as the biosafety issues of their clinical application are yet to be fully evaluated. Further improvement of antimicrobial activity to reduce the usage, and thus reduce the potential risk, is an important way to increase the clinical applicability of antibacterial nanomaterials.

In this paper, an antimicrobial nanostructure with both the photothermal effect and peroxidase-like activity was constructed to combine the photothermal antimicrobial and free radical antimicrobial strategies to achieve efficient synergistic antimicrobial activity (Scheme 1). ZIF-8, a frequently used metal-organic framework (MOF) in biomedical research, was chosen as the nanocarrier. A PDA layer with an excellent

photothermal effect was encapsulated on the surface of ZIF-8 by *in situ* polymerization, and then, platinum nanoparticles (PtNPs) with peroxidase-like activity were allowed to grow on the PDA layer. The obtained nano-antimicrobial agent (ZIF-8@PDA@Pt) can not only efficiently catalyze the production of ROS from H₂O₂ to cause damage to bacteria but also convert photon energy of the near-infrared light into thermal energy to kill bacteria, and the two synergistic effects induced in a highly efficient antimicrobial activity.

2 Materials and methods

2.1 Synthesis of ZIF-8@PDA@Pt

ZIF-8 was synthesized through a specific coordination reaction between zinc ions and 2-methylimidazole. In a typical experiment, 1.069 g Zn(NO₃)₂·6H₂O was dissolved in 15 mL of DMF-MeOH mixture (v/v = 4:1) as solution 1, 1.161 g of 2-methylimidazole was dissolved in 10 mL of DMF-MeOH (v/v = 4:1) as solution 2; then, solution 1 was added to solution 2 and kept stirring vigorously overnight. Subsequently, the milky product was collected by centrifugation at 14,000 rpm for 10 min, rinsed with methanol and ultrapure water two times, and then dried at 80°C overnight to obtain ZIF-8 for subsequent experiments.

ZIF-8@PDA was attained by a self-polymerization reaction of dopamine. A measure of 20 mg ZIF-8 we prepared was dissolved in the Tris-HCl buffer solution (pH 8.5, 50 mM) with the assistance of sonicating for 2 min; then, 10 mg dopamine was added to the above solution, and the mixture was violently stirred for 90 min. Thereafter, the obtained black mixture was collected by centrifugation at 14,000 rpm for 10 min, washed with water three times, and eventually concentrated to 2 mL for later use.

Subsequently, ZIF-8@PDA@Pt was gained by an *in situ* reduction method using ZIF-8@PDA as a precursor. A measure of 2 mL of ZIF-8@PDA we prepared previously was added to 7,740 μ L ultrapure water and sonicated for 2 min; then, 260 μ L of H₂PtCl₄ (19.2 mM) was added and sonicated for 5 min; in a rapid subsequence, 500 μ L of the refresh NaBH₄ solution (1 M) was added to the above solution under drastic magnetic stirring for 1 h. Finally, the mixture was collected by centrifugation at 14,000 rpm for 10 min and ultimately washed with ultrapure water three times to obtain ZIF-8@PDA@Pt.

2.2 Measurement of peroxidase-mimic activity

The peroxidase-mimic activity of ZIF-8@PDA@Pt was measured by a classical chromogenic reaction using TMB as the substrate. In brief, 5 μ L TMB (80 mM), 50 mL H₂O₂ (10 mM), and 50 μ L ZIF-8@PDA@Pt (0.2 mg mL⁻¹) were added to the phosphate buffer solution (pH 5.0, 20 mM) with a total volume of 0.5 mL, respectively. Subsequently, the mixture was incubated for 5 min, and the absorbance at 652 nm was recorded simultaneously by an ultraviolet-visible spectrum. o-Phenylenediamine (OPD) was employed as a chromogenic substrate to further evaluate the peroxidase-mimic activity of ZIF-8@PDA@Pt. Typically, 5 μ L OPD (50 mM), 50 mL H₂O₂ (10 mM), and 50 μ L ZIF-8@PDA@

Pt (0.2 mg mL⁻¹) were added to the phosphate buffer solution (pH 5.0, 20 mM) with a total volume of 0.5 mL, respectively. Subsequently, the mixture was incubated for 5 min, and the absorbance at 425 nm was recorded simultaneously by an ultraviolet-visible spectrum.

2.3 Catalytic kinetic assay

The kinetic assay of the peroxidase-mimic activity of ZIF-8@PDA@Pt was conducted by changing the concentration of H₂O₂ or TMB. The reaction was performed under an optimized condition (pH 5.0, 37°C). Typically, 2 μL TMB (80 mM), H₂O₂ with different concentrations, and 20 μL ZIF-8@PDA@Pt (0.2 mg mL⁻¹) were added to a phosphate buffer solution (pH 5.0, 20 mM) with a total volume of 0.2 mL; then, the absorbance at 652 nm was recorded in time at a time scanning window. The real-time velocity of the reaction was converted by the Beer–Lambert Law, $A = \epsilon bC$, where b is the path length (1 cm) and ϵ is the molar absorption coefficient of oxidized TMB (39,000 M⁻¹ cm⁻¹). Corresponding parameters of kinetics were calculated according to the Michaelis–Menten equation and Lineweaver–Burk plot:

$$V_0 = V_{max} \frac{[S]}{[S] + K_m},$$

$$\frac{1}{V_0} = \frac{K_m}{V_{max}} \frac{1}{[S]} + \frac{1}{V_{max}},$$

where V_0 is the initial reaction rate and $[S]$ is the concentration of the substrate (H₂O₂ or TMB).

2.4 Detection of ROS generation

Terephthalic acid (TA) was used as a fluorescent probe to validate the generation of •OH. Typically, TA (0.5 mM), H₂O₂ (2 mM), and ZIF-8@PDA@Pt (0.1 mg mL⁻¹) were first mixed into PBS (pH = 5.0, 20 mM) and incubated in dark for 2 h, and then were taken for fluorescent spectra characterization. In addition, 1,3-diphenylisobenzofuran (DPBF) and 9,10-anthracenediyl-bis(methylene)-dimalonic acid (ABDA) were used as probes to assay O₂^{•-} and ¹O₂, respectively. Specifically, DPBF (1 mM), H₂O₂ (2 mM), and ZIF-8@PDA@Pt (0.1 mg mL⁻¹) were incubated together in PBS (pH = 5.0, 20 mM) for 5 min; meanwhile, the absorbance at 421 nm was recorded every 30 s. ABDA (0.05 mM), H₂O₂ (2 mM), and ZIF-8@PDA@Pt (0.1 mg mL⁻¹) were incubated together in PBS (pH = 5.0, 20 mM) for a while and then were taken to measure the change of absorbance using UV spectra.

2.5 Determination of the photothermal property

The photothermal property of ZIF-8@PDA@Pt was determined using an 808-nm laser, and the real-time temperature was observed with a thermal imaging camera. In brief, ZIF-8@PDA@Pt aqueous dispersion with different concentrations (0, 20, 40, 60, 80, 100, and

120 μg mL⁻¹) was radiated under 808 nm (1.0 W cm⁻²) for 5 min. Concurrently, the temperature of the ZIF-8@PDA@Pt aqueous dispersion was recorded every 30 s. Thereafter, the heating–cooling curves were obtained to calculate the photothermal conversion efficiency in accordance with below equations:

$$\eta = \frac{hS(T_{max} - T_{surr}) - Q_0}{I(1 - 10^{-A_{808}})}, \quad (1)$$

$$\tau_s = \frac{m_d C_d}{hS}, \quad (2)$$

$$Q_0 = hS(T_{max,water} - T_{surr}), \quad (3)$$

where η is the photothermal conversion efficiency. The value of τ_s was obtained by linearly fitting the plot of the cooling time t versus the term $-\ln\theta$, hS was obtained from Eq. 2, m_d is the mass of the solution (0.2 g), C_d is the heat capacity of water (4.2 J g⁻¹°C⁻¹), Q_0 was obtained from Eq. 3, T_{max} is the equilibrium temperature (61.5°C), $T_{max,water}$ is the maximum temperature of water (29.1°C), and T_{surr} is the surrounding ambient temperature (28.3°C). I is the incident light power (0.8 W cm⁻²), and A_{808} is the absorbance of the ZIF-8@PDA@Pt aqueous dispersion (120 μg mL⁻¹) at 808 nm (0.17).

2.6 Antibacterial activity test

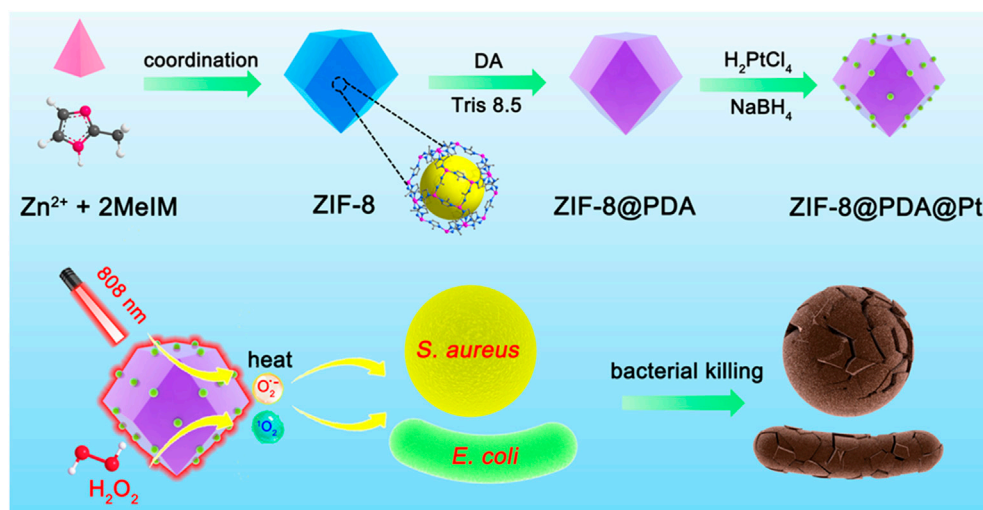
Staphylococcus aureus and *Escherichia coli* were selected as Gram-positive and Gram-negative model strains to estimate the antibacterial activity of ZIF-8@PDA@Pt, respectively. Mono colonies of *S. aureus* and *E. coli* on a solid agar plate were first transferred to 2 mL of the lysogeny broth (LB) medium and shaken at 37°C for 12 h at 150 rpm. Four different groups were set in this typical procedure, containing I: Control, II: H₂O₂, III: ZIF-8@PDA@Pt + H₂O₂, and IV ZIF-8@PDA@Pt + H₂O₂ + NIR. In addition, 0.3 was selected as the initial optical density of bacteria at OD_{600 nm}. In addition, the final concentration of H₂O₂ and ZIF-8@PDA@Pt in the incubation system was 2 mM and 100 μg mL⁻¹, respectively. All groups were incubated at 37°C for 20 min. Thereafter, the bacterial suspensions were moved to the solid medium by the spread plate method and cultured at 37°C for another for 12 h. Finally, all experimental groups were taken for imaging and counting. Each assay was performed in triplicates.

2.7 Live/dead bacterial staining

Bacterial suspensions treated with the different experimental conditions were first centrifuged for 5 min (4,000 rpm), followed by washing two times using 0.85% NaCl solutions. Afterward, the above bacterial suspensions were stained with SYTO 9 and propidium iodide and then observed with a fluorescent microscope.

2.8 Cell viability assay

HSF cells were performed for the biocompatibility assay of ZIF-8@PDA@Pt. At first, the HSF cells were cultured in a 96-well plate (8,000 cells per well) at 37°C for 24 h; then, ZIF-8@PDA@Pt with



SCHEME 1
Schematic illustration of the synthesis of ZIF-8@PDA@Pt and the principle of bacterial killing.

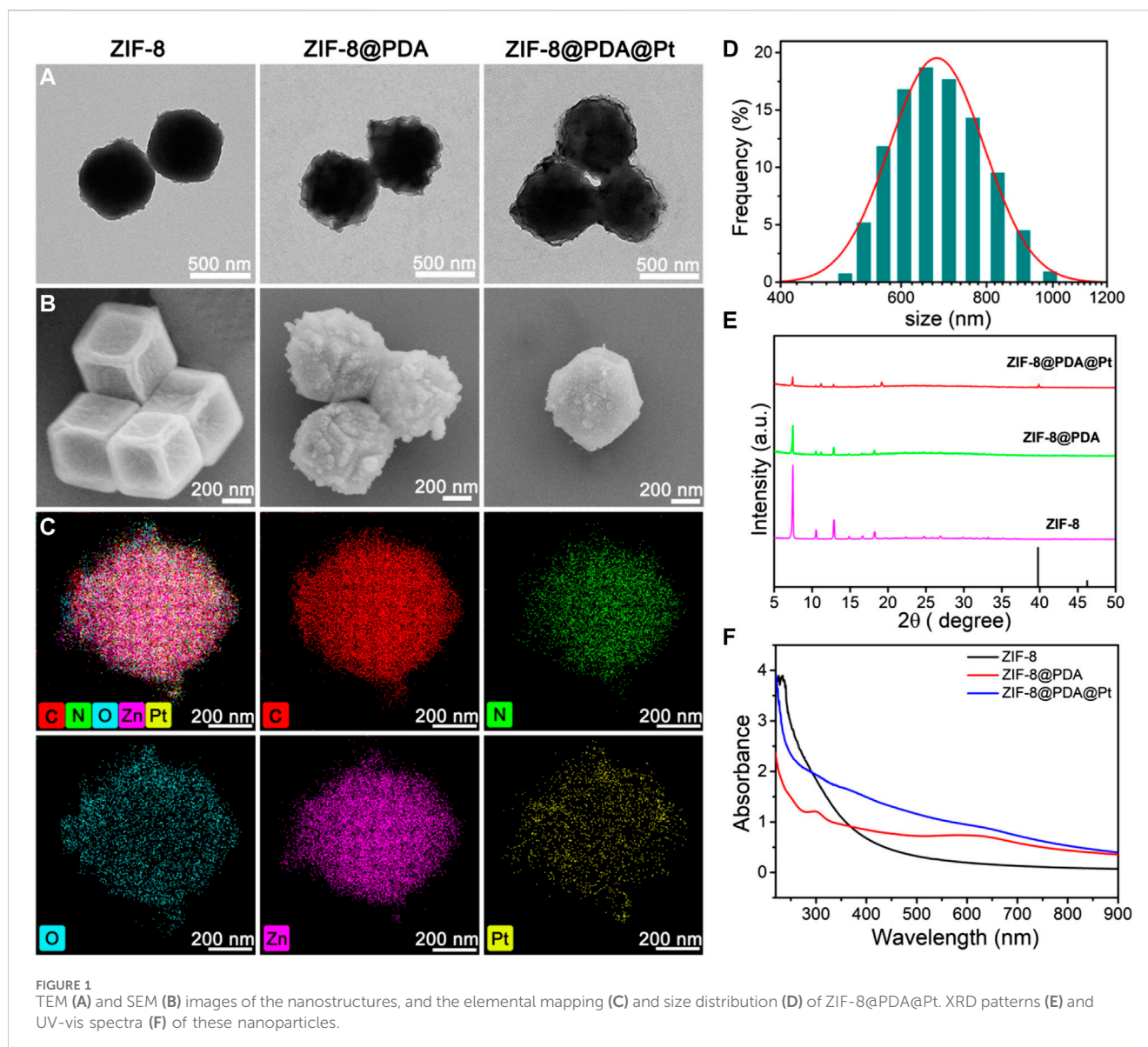
different concentrations (0, 25, 50, 100, 150, and 200 $\mu\text{g mL}^{-1}$) were added to the above medium and incubated for another 24 h at 37°C. Thereafter, 10 μL of the MTT solution was added to every well. After 4 h, the medium was extracted and 150 μL of DMSO was added to every well. The cell viability was assayed using a microplate reader.

3 Results and discussion

3.1 Synthesis and characterization of ZIF-8@PDA@Pt

ZIF-8@PDA@Pt was prepared through *in situ* reduction of H_2PtCl_4 in the presence of a specific precursor obtained by modifying a layer of polydopamine on the surface of ZIF-8. To begin with, ZIF-8 was conducted by a specific coordination reaction between zinc ions and 2-methylimidazole. Afterward, a layer of PDA was modified on ZIF-8, relying on the self-polymerization reaction of dopamine under a weak alkaline environment to obtain ZIF@PDA. Eventually, Pt NPs were localized on ZIF@PDA by *in situ* reduction to obtain the nanozyme ZIF-8@PDA@Pt. TEM and SEM were primarily employed to characterize the morphology during the formation of ZIF-8@PDA@Pt (Figures 1A, B); it is clearly to be observed that ZIF-8 possesses the regular rhombic dodecahedral morphology while a thin layer at the edge of ZIF-8 was noticed after modifying polydopamine, verifying the formation of ZIF-8@PDA. In addition, it can be seen that ultra-small Pt NPs were distributed on ZIF-8@PDA. In addition, energy-dispersive X-ray spectrometry (EDX) mapping was recruited to characterize the elemental distribution of ZIF-8@PDA@Pt nanozyme (Figure 1C). The results presented the homogeneous distributions of elements C, N, O, Zn, and Pt in ZIF-8@PDA@Pt, demonstrating the successful loading of Pt NPs onto the ZIF-8@PDA platform. Meanwhile, ZIF-8@PDA@Pt exhibits a size of approximately 650 nm, according to the dynamic light scattering analysis (Figure 1D).

Additionally, in order to explore the chemical structure and composition, we executed X-ray diffraction (XRD), X-ray photoelectron spectroscopy (XPS), and UV-vis spectra. As illustrated in Figure 1E, the pattern of ZIF-8 exhibits several typical characteristic peaks at around 7.46°, 10.52°, 12.87°, and 18.27°, ascribing to (001), (002), (112), and (222) crystal faces, respectively, which conforms its regular crystal structure. Of note, the main diffraction peaks of ZIF-8 remained after modifying PDA and loading Pt NPs. In particular, the XRD diffraction of ZIF-8@PDA@Pt presents an unmistakable peak at 39.5° in line with the (111) facet of the Pt crystal (JCPDS No. 04-0802), which further confirmed the successful preparation of ZIF-8@PDA@Pt. The UV-vis spectra were also measured and are presented in Figure 1F. It can be noted that two typical peaks at approximately 234 and 300 nm in ZIF-8 and ZIF-8@PDA assigned to the $\pi\text{-}\pi^*$ transition of the conjugated system from the imidazole structure and $n\text{-}\pi^*$ transition of polydopamine, respectively. Nonetheless, the peak at approximately 300 nm is not well-preserved in ZIF-8@PDA@Pt, which may be caused within the loading of Pt NPs. In addition, XPS was performed to characterize the element constitution of ZIF-8@PDA@Pt (Supplementary Figure S1). The element contents of C, N, O, Zn, and Pt are 53.08%, 9.55%, 25.03%, 10.72%, and 1.62%, respectively. More precisely, in the high-resolution spectrum of Pt 4f, the peaks located at 71.0, 72.2, 74.2, and 75.5 eV are ascribed to Pt^0 4f 7/2, Pt^{4+} 4f 7/2, Pt^0 4f 5/2, and Pt^{4+} 4f 5/2 binding energies, respectively, which are analogous to the majority of Pt NPs. Likewise, several typical peaks at approximately 284.5, 286.2, and 288.3 eV can be identified from the high-resolution C1s spectrum, which are assigned to C-C, C-N/C-O, and C=C groups, respectively. It can be observed that three peaks are located at 398.2, 399.3, and 400.7 eV from the N 1s spectrum, corresponding to pyridinic N, pyrrolic N, and graphitic N, respectively. Comparably, the curve-fitted O1s spectrum exhibits two peaks 531.3 and 533.1 eV, attributing to C-O and C-OH groups, respectively. In addition, the high-resolution Zn 2p spectra of ZIF-8@PDA@Pt present two peaks

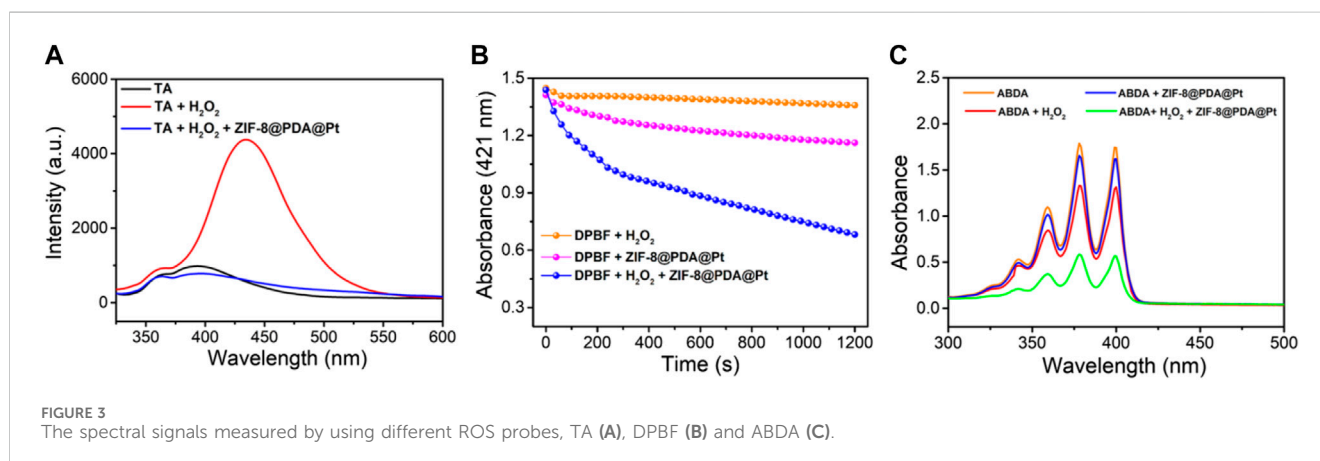
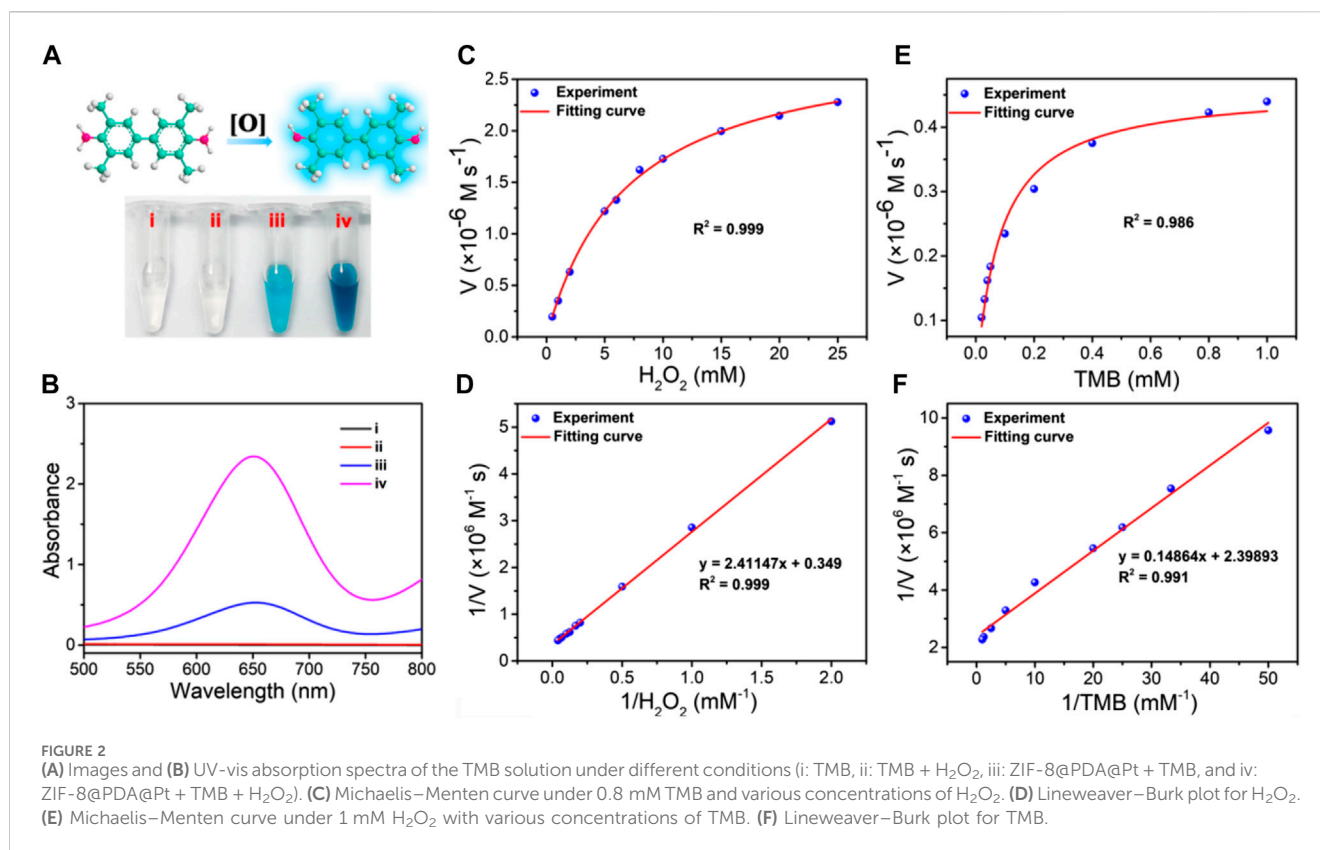


placed at 1022.3 and 1045.3 eV belonging to Zn 2p 1/2 and Zn 2p 2/3 of zinc oxide, respectively. In combination with the above results, it is believed that ZIF-8@PDA@Pt was successfully prepared.

3.2 Catalytic performance of ZIF-8@PDA@Pt

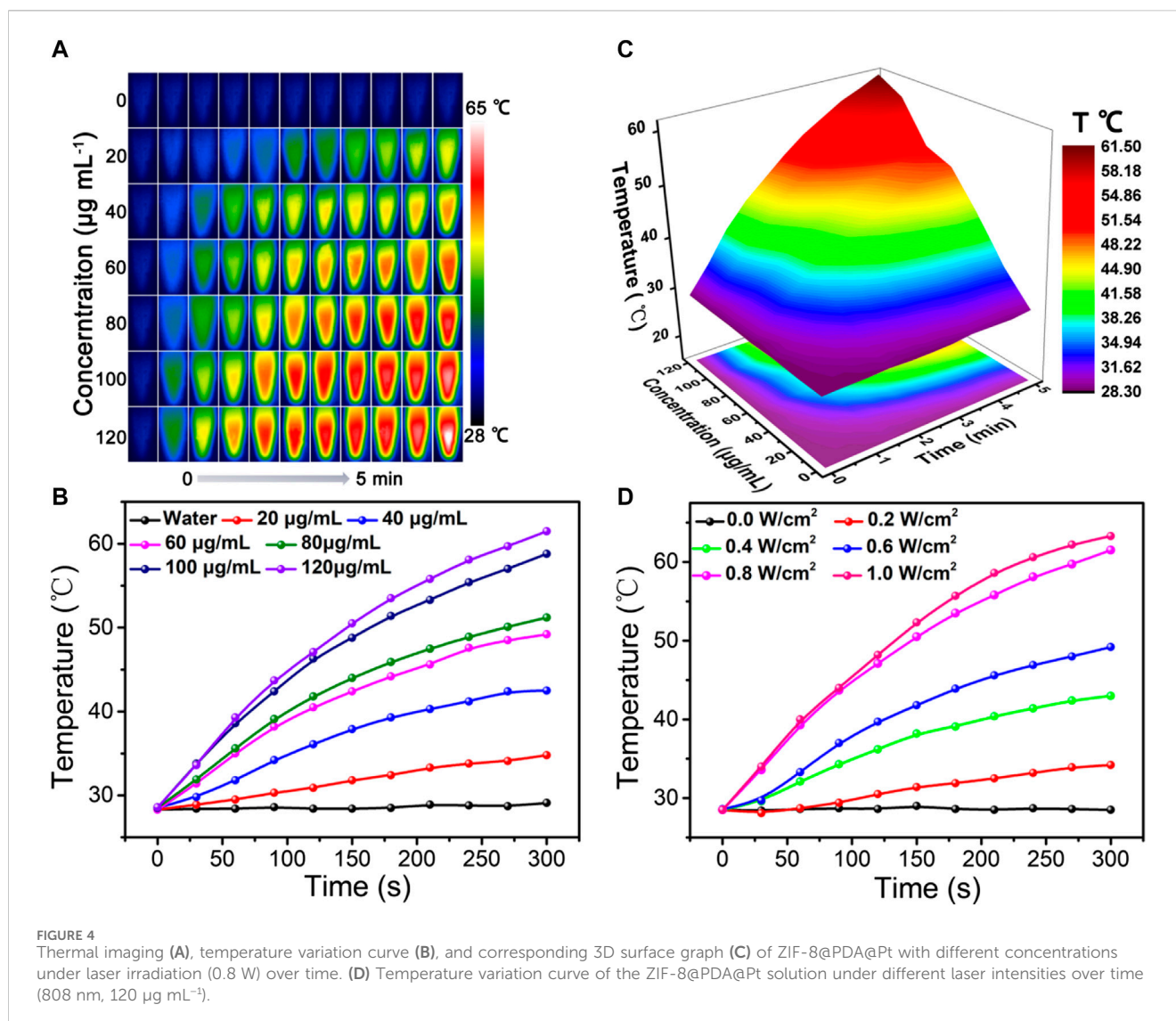
After successful synthesis of the ZIF-8@PDA@Pt nanoparticles, we then investigated its peroxidase (POD)-like activity using 3,3',5,5'-tetramethylbenzidine (TMB) as the chromogenic substrate and H₂O₂ as the catalysis substrate. As shown in Figure 2A, without ZIF-8@PDA@Pt, H₂O₂ cannot cause any color change in the TMB solution. However, in the presence of ZIF-8@PDA@Pt and H₂O₂, the color of the TMB solution significantly changed to dark blue (Figures 2A–2iv), indicating the strong POD-like activity of ZIF-8@PDA@Pt. In this catalytic system, ZIF-8@PDA@Pt may catalyze H₂O₂ to produce ROS, which can oxidize TMB to generate blue color. Notably, without H₂O₂, the

nanozyme ZIF-8@PDA@Pt can also cause an obvious change in the color of the TMB solution (Figures 2A–2iii), demonstrating that the nanozyme also possesses oxidase-like activity. The enzyme-like activity of ZIF-8@PDA@Pt was also demonstrated from the absorbance change of the TMB solution (Figure 2B). To further evaluate the enzymatic activities of the nanozyme ZIF-8@PDA@Pt, the catalytic dynamics was investigated. We carried out a steady-state kinetic study to obtain the rate constants by varying the concentration of TMB with a constant concentration of H₂O₂ or *vice versa*. The Michaelis constant (K_m) and maximum reaction rate (V_{max}) were calculated from the fitted Michaelis–Menten curves and Lineweaver–Burk double reciprocal plots (Figures 2C–F). As a comparison, the obtained K_m and V_{max} of ZIF-8@PDA@Pt and other catalysts including the natural enzyme HRP and Fe₃O₄ nanozymes are listed in Supplementary Table S1. K_m indicates the enzyme affinity toward substrates, and V_{max} defines the maximal catalytic capacity of an enzyme under specified conditions. Generally, a smaller K_m demonstrates higher affinity,



while the higher V_{\max} refers to the better catalytic capability. These results indicated that the obtained nanozyme ZIF-8@PDA@Pt shows better catalytic performance than the classical POD nanozyme Fe₃O₄, and some parameters are even significantly better than natural enzymes. For example, K_m of ZIF-8@PDA@Pt was 0.062 mM for TMB, which is much lower than that of HRP and Fe₃O₄, indicating that ZIF-8@PDA@Pt has the highest enzyme affinity toward TMB. Moreover, ZIF-8@PDA@Pt also shows the highest V_{\max} values. These results demonstrated that the obtained ZIF-8@PDA@Pt possesses excellent POD-like activity, also implying the strong ROS generation ability of the ZIF-8@PDA@Pt–H₂O₂ system.

To further verify the ability of ZIF-8@PDA@Pt to catalyze the production of different free radicals from H₂O₂, terephthalic acid (TA), 1,3-diphenylisobenzofuran (DPBF), and 9,10-anthracenediylbis(methylene)-dimalonic acid (ABDA) were chosen as the indicators for the sensing of hydroxyl radical ($\bullet\text{OH}$), O₂^{•−} (superoxide anion), and singlet oxygen (¹O₂), respectively. TA is a non-fluorescent molecule that can be oxidized by $\bullet\text{OH}$ to generate blue fluorescence. DPBF is a fluorescent molecule which possesses a specific reactivity toward ¹O₂ and O₂^{•−}, forming an endoperoxide that can decompose to give 1,2-dibenzoylbenzene. This decomposition of DPBF by ¹O₂ and O₂^{•−} can be measured by the decrease in the absorbance intensity of DPBF at 412 nm. ABDA is a



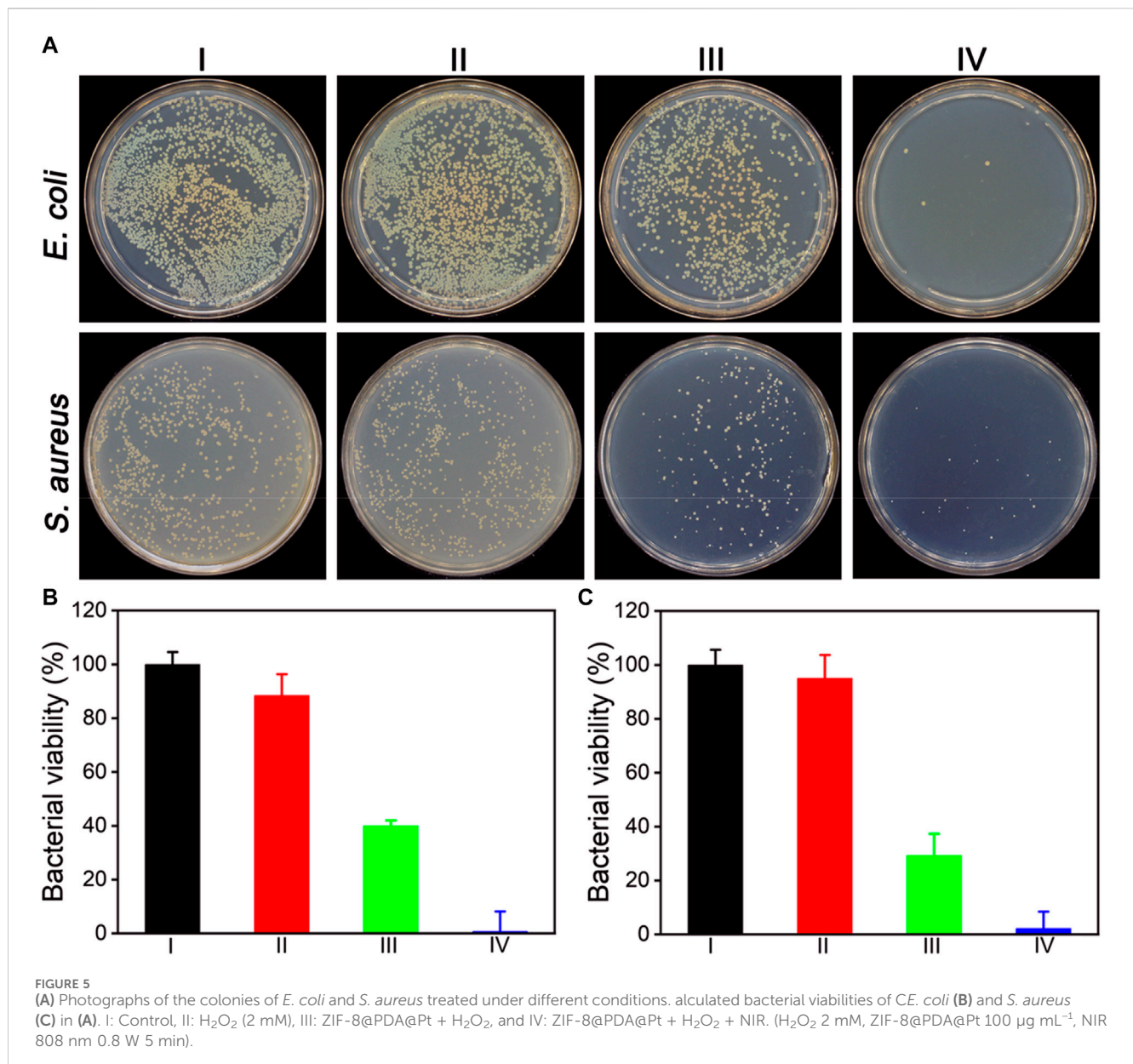
highly selective probe for singlet oxygen $^1\text{O}_2$, which can be oxidized with the decrease in the absorbance intensity. As shown in Figure 3, in the solution with the probes and H_2O_2 , the presence of ZIF-8@PDA@P can induce significant sensing signals of $\bullet\text{OH}$, $\text{O}_2^{\bullet-}$, and $^1\text{O}_2$. These results strongly demonstrated that ZIF-8@PDA@Pt can catalyze the production of different free radical species from H_2O_2 , which is very important for bacterial disinfection.

3.3 Photothermal effect of ZIF-8@PDA@Pt

As illustrated in the UV-vis spectra of Figure 1F, ZIF-8@PDA@Pt presents broad and intense adsorption from the ultraviolet to NIR region, manifesting ZIF-8@PDA@Pt possesses considerable photothermal conversion potential. So as to validate the supposition, the photothermal property of ZIF-8@PDA@Pt was primarily investigated, where the aqueous dispersions of ZIF-8@PDA@Pt with different concentrations were irradiated under an 808-nm NIR laser. Simultaneously, the real-time temperatures were recorded by a thermal imaging camera. It can be observed from

Figures 4A–C that the temperature of the aqueous solution lifted promptly with the augment of the concentration of ZIF-8@PDA@Pt and the prolongation of irradiation time. Indeed, the constant arising trend of the curve implied that ZIF-8@PDA@Pt exhibits supreme photostability under the irradiation of the NIR laser. It can also be visually discovered from the quantitative data that the temperature of the ZIF-8@PDA@Pt solution (120 $\mu\text{g mL}^{-1}$) elevated rapidly from 28.5°C to 61.5°C within 5 min of irradiation, while the temperature of water only raised by 0.8°C under the same conditions. Such a result elucidated ZIF-8@PDA@Pt can serve as a remarkable photothermal agent. Hence, we further calculated the photothermal conversion efficiency of ZIF-8@PDA@Pt in line with a method reported previously (Supplementary Figure S2), where it can be up to 65.4% to our surprise, and this excellent property just met the experimental results we obtained as well, where the real-time temperature of the NIR-irradiated ZIF-8@PDA@Pt aqueous solution can reach up to 61.5°C in a short time.

In addition, it was found that ZIF-8@PDA@Pt presented a laser power-dependent behavior. As shown in Figure 4D, the temperature of solutions at the same time nodes increased gradually along with

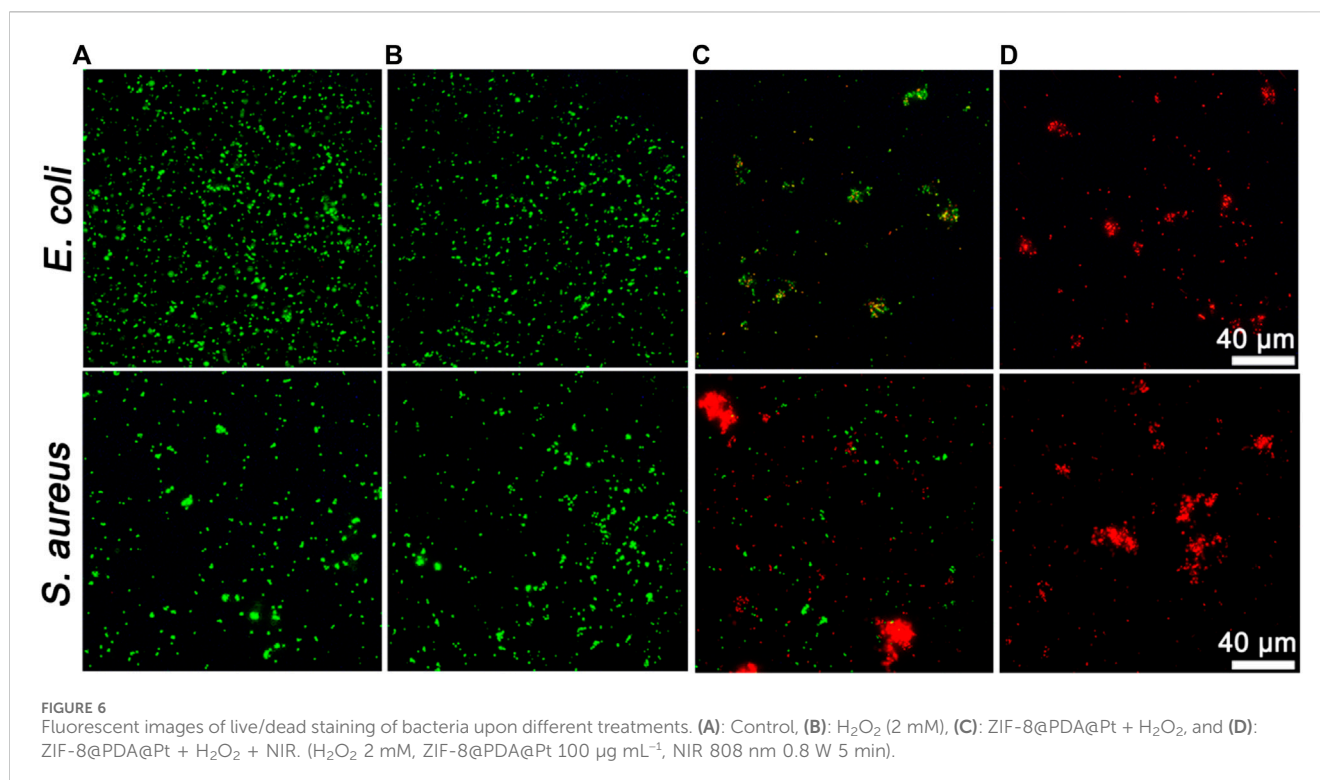


the increase in laser power, denoting the laser power to be imperative to the photothermal conversion ability of ZIF-8@PDA@Pt. Afterward, the thermal stability of ZIF-8@PDA@Pt was estimated by photothermal performance cycle monitoring within four laser cycles. It can be noted from [Supplementary Figure S3](#) that there were no unmistakable temperature fluctuations in the four photothermal cycles, demonstrating ZIF-8@PDA@Pt endows considerable photothermal stability. All above results certified that ZIF-8@PDA@Pt possessed excellent photothermal properties, which can support its application for sterilization.

3.4 Synergistic antibacterial effect of ZIF-8@PDA@Pt

Inspired by the superior enzymatic activity and photothermal property of ZIF-8@PDA@Pt, the *in vitro* synergistic antibacterial

effect of ZIF-8@PDA@Pt against Gram-negative bacteria (*E. coli*) and Gram-positive bacteria (*S. aureus*) was assessed by the plate counting method. As shown in [Figure 5](#), H_2O_2 (2 mM) alone cannot induce significant influence on the bacterial viability. However, in the presence of ZIF-8@PDA@Pt, the viabilities of both *E. coli* and *S. aureus* decreased to below 40%. The ROS generated from H_2O_2 under the catalysis of ZIF-8@PDA@Pt would be responsible for this sharp decrease in the bacterial viability. Moreover, as expected, NIR irradiation greatly promoted the antibacterial efficiency of the ZIF-8@PDA@Pt/ H_2O_2 system, in which the bacterial viabilities decreased to below 3%. The viability of the treated bacteria was also investigated by a live/dead staining kit, which contains two dyes, SYTO 9 and propidium iodide (PI). SYTO 9 is a membrane-permeable dye that can give a green fluorescence to indicate the live cells due to the binding with bacterial nucleic acid. PI is also a nucleic acid-binding dye used to give a red



fluorescence, which can only penetrate the damaged membrane of dead bacteria. As shown in [Figure 6](#), upon treating with ZIF-8@PDA@Pt and H₂O₂, significant amount of dead bacteria was found in the fluorescence images, and almost all of the bacteria were killed when the ZIF-8@PDA@Pt/H₂O₂ system was irradiated with the NIR light. This phenomenon was the same as that found in the plate counting experiments. These results clearly demonstrated the high synergistic antimicrobial activity of the nanozyme ZIF-8@PDA@Pt in the presence of H₂O₂ and NIR light irradiation. Notably, the nanozyme also has good biocompatibility; in the MTT assay, over 90% of the HSF cells remain alive when in the incubation with 250 μg mL⁻¹ of ZIF-8@PDA@Pt.

4 Conclusion

In conclusion, a platinum nanozyme ZIF-8@PDA@Pt with high peroxidase-like activity was successfully synthesized. The catalytic activity is much higher than the classical nanozyme Fe₃O₄, and some parameters are even better than the natural enzyme HRP. The obtained nanozyme ZIF-8@PDA@Pt can efficiently promote the generation of different ROS from H₂O₂. Moreover, ZIF-8@PDA@Pt can harvest the photon energy from the NIR light to heating the solution. The combined excellent photothermal effect and peroxidase-like activity resulted in high synergistic antimicrobial activity of the nanozyme ZIF-8@PDA@Pt in the presence of H₂O₂ and NIR light irradiation. The developed nano-antibacterial strategy is highly promising for wide applications, for example, wound infection treatment, antibacterial coatings for medical materials, preservation and protection of agricultural products, etc.

Data availability statement

The original contributions presented in the study are included in the article/[Supplementary Material](#); further inquiries can be directed to the corresponding authors.

Author contributions

XL: methodology, writing–review and editing, investigation, and writing–original draft. WZ: writing–review and editing, investigation, methodology, and writing–original draft. YZ: investigation, methodology, and writing–review and editing. NW: investigation, methodology, and writing–review and editing. XG: investigation, methodology, and writing–original draft. SS: methodology and writing–review and editing. MC: investigation and writing–review and editing. ZZ: methodology, conceptualization, funding acquisition, supervision, writing–original draft, and writing–review and editing. GH: methodology, funding acquisition, supervision, and writing–review and editing.

Funding

The author(s) declare that financial support was received for the research, authorship, and/or publication of this article. This research received financial support from the National Natural Science Foundation of China (NSFC) (No. 22007083), China Agriculture Research System (CARS-29), and the Fundamental Research Funds of the Shengzhou Innovation Research Institute of Zhejiang Sci-Tech University (No. SY Y 2023B000004). The Program of Agricultural Product Quality Safety Risk Assessment (GJFP20210501).

Conflict of interest

The authors declare that the research was conducted in the absence of any commercial or financial relationships that could be construed as a potential conflict of interest.

Publisher's note

All claims expressed in this article are solely those of the authors and do not necessarily represent those of their affiliated

organizations, or those of the publisher, the editors, and the reviewers. Any product that may be evaluated in this article, or claim that may be made by its manufacturer, is not guaranteed or endorsed by the publisher.

Supplementary material

The Supplementary Material for this article can be found online at: <https://www.frontiersin.org/articles/10.3389/fbioe.2024.1355004/full#supplementary-material>

References

- Chen, Z., Wang, Z., Ren, J., and Qu, X. (2018). Enzyme mimicry for combating bacteria and biofilms. *Accounts Chem. Res.* 51, 789–799. doi:10.1021/acs.accounts.8b00011
- Dorma Momo, C., Zhou, Y., Li, L., Zhu, W., Wang, L., Liu, X., et al. (2022). A metal-organic framework nanocomposite with oxidation and near-infrared light cascade response for bacterial photothermal inactivation. *Front. Chem.* 10, 1044931. doi:10.3389/fchem.2022.1044931
- Du, Q., Wu, X., Bi, W., Xing, B., and Yeow, E. K. L. (2021). Increasing antibiotic activity by rapid bioorthogonal conjugation of drug to resistant bacteria using an upconverted light-activated photocatalyst. *J. Mater. Chem. B* 9, 3136–3142. doi:10.1039/d0tb02568b
- Fan, C., Zhao, J., Tang, Y., and Lin, Y. (2023). Using near-infrared I/II light to regulate the performance of nanozymes. *J. Analysis Test.* 7, 272–284. doi:10.1007/s41664-023-00257-z
- Fu, B., Liu, Q., Liu, M., Chen, X., Lin, H., Zheng, Z., et al. (2022). Carbon dots enhanced gelatin/chitosan bio-nanocomposite packaging film for perishable foods. *Chin. Chem. Lett.* 33, 4577–4582. doi:10.1016/j.ccl.2022.03.048
- Guo, C., Zhang, J., Feng, X., Du, Z., Jiang, Y., Shi, Y., et al. (2022). Polyhexamethylene biguanide chemically modified cotton with desirable hemostatic, inflammation-reducing, intrinsic antibacterial property for infected wound healing. *Chin. Chem. Lett.* 33, 2975–2981. doi:10.1016/j.ccl.2021.12.086
- Han, Q., Lau, J. W., Do, T. C., Zhang, Z., and Xing, B. (2020). Near-infrared light brightens bacterial disinfection: recent progress and perspectives. *ACS Appl. Bio Mater.* 4, 3937–3961. doi:10.1021/acsabm.0c01341
- Hu, H., Kang, X., Shan, Z., Yang, X., Bing, W., Wu, L., et al. (2022). A DNase-mimetic artificial enzyme for the eradication of drug-resistant bacterial biofilm infections. *Nanoscale* 14, 2676–2685. doi:10.1039/d1nr07629a
- Huang, Q., Zhu, W., Gao, X., Liu, X., Zhang, Z., and Xing, B. (2023). Nanoparticles-mediated ion channels manipulation: from their membrane interactions to bioapplications. *Adv. Drug Deliv. Rev.* 195, 114763. doi:10.1016/j.addr.2023.114763
- Ikuta, K. S., Swetschinski, L. R., Robles Aguilar, G., Sharara, F., Mestrovic, T., Gray, A. P., et al. (2022). Global mortality associated with 33 bacterial pathogens in 2019: a systematic analysis for the Global Burden of Disease Study 2019. *Lancet* 400, 2221–2248. doi:10.1016/s0140-6736(22)02185-7
- Jiao, L., Li, Q., Li, C., Gu, J., Liu, X., He, S., et al. (2023). Orthogonal light-triggered multiple effects based on photochromic nanoparticles for DNA cleavage and beyond. *J. Mater. Chem. B* 11, 2367–2376. doi:10.1039/d2tb02638d
- Li, L., Zhou, Y., Li, P., Xu, Q., Li, K., Hu, H., et al. (2022b). Peptide hydrogel based sponge patch for wound infection treatment. *Front. Bioeng. Biotechnol.* 10, 1066306. doi:10.3389/fbioe.2022.1066306
- Li, Y., Zheng, H., Liang, Y., Xuan, M., Liu, G., and Xie, H. (2022a). Hyaluronic acid-methacrylic anhydride/polyhexamethylene biguanide hybrid hydrogel with antibacterial and proangiogenic functions for diabetic wound repair. *Chin. Chem. Lett.* 33, 5030–5034. doi:10.1016/j.ccl.2022.03.116
- Liu, J., Liu, X., Yang, L., Cai, A., Zhou, X., Zhou, C., et al. (2022a). A highly sensitive electrochemical cytosensor based on a triple signal amplification strategy using both nanozyme and DNzyme. *J. Mater. Chem. B* 10, 700–706. doi:10.1039/d1tb02545g
- Liu, S., Xu, J., Xing, Y., Yan, T., Yu, S., Sun, H., et al. (2022b). Nanozymes as efficient tools for catalytic therapeutics. *VIEW* 3, 20200147. doi:10.1002/viw.20200147
- Makabenta, J. M. V., Nabawy, A., Li, C.-H., Schmidt-Malan, S., Patel, R., and Rotello, V. M. (2021). Nanomaterial-based therapeutics for antibiotic-resistant bacterial infections. *Nat. Rev. Microbiol.* 19, 23–36. doi:10.1038/s41579-020-0420-1
- Murray, C. J. L., Ikuta, K. S., Sharara, F., Swetschinski, L., Robles Aguilar, G., Gray, A., et al. (2022). Global burden of bacterial antimicrobial resistance in 2019: a systematic analysis. *Lancet* 399, 629–655. doi:10.1016/s0140-6736(21)02724-0
- Niu, J., Sun, Y., Wang, F., Zhao, C., Ren, J., and Qu, X. (2018). Photomodulated nanozyme used for a gram-selective antimicrobial. *Chem. Mater.* 30, 7027–7033. doi:10.1021/acs.chemmater.8b02365
- Niu, J., Wang, L., Cui, T., Wang, Z., Zhao, C., Ren, J., et al. (2021a). Antibody mimics as bio-orthogonal catalysts for highly selective bacterial recognition and antimicrobial therapy. *ACS Nano* 15, 15841–15849. doi:10.1021/acsnano.1c03387
- Niu, J., Zhao, C., Liu, C., Ren, J., and Qu, X. (2021b). Bio-inspired bimetallic enzyme mimics as bio-orthogonal catalysts for enhanced bacterial capture and inhibition. *Chem. Mater.* 33, 8052–8058. doi:10.1021/acs.chemmater.1c02469
- Sun, Y., Zhao, C., Niu, J., Ren, J., and Qu, X. (2020). Colorimetric band-aids for point-of-care sensing and treating bacterial infection. *ACS Central Sci.* 6, 207–212. doi:10.1021/acscentsci.9b01104
- Wang, W., Li, P., Huang, Q., Zhu, Q., He, S., Bing, W., et al. (2023). Functionalized antibacterial peptide with DNA cleavage activity for enhanced bacterial disinfection. *Colloids Surfaces B Biointerfaces* 228, 113412. doi:10.1016/j.colsurfb.2023.113412
- Wang, Y., Zhang, C., Zhang, H., Feng, L., and Liu, L. (2022). A hybrid nano-assembly with synergistically promoting photothermal and catalytic radical activity for antibacterial therapy. *Chin. Chem. Lett.* 33, 4605–4609. doi:10.1016/j.ccl.2022.03.076
- Wang, Z., Zhen, X., Upputuri, P. K., Jiang, Y., Lau, J., Pramanik, M., et al. (2019). Redox-activatable and acid-enhanced nanotheranostics for second near-infrared photoacoustic tomography and combined photothermal tumor therapy. *ACS Nano* 13, 5816–5825. doi:10.1021/acsnano.9b01411
- Wu, T., Fu, Y., Guo, S., Shi, Y., Zhang, Y., Fan, Z., et al. (2023). Self-assembly multifunctional DNA tetrahedron for efficient elimination of antibiotic-resistant bacteria. *Aggregate*, e402. doi:10.1002/agt.2.402
- Wu, X., and Yeow, E. K. L. (2022). Exploiting the upconversion luminescence, Lewis acid catalytic and photothermal properties of lanthanide-based nanomaterials for chemical and polymerization reactions. *Phys. Chem. Chem. Phys.* 24, 11455–11470. doi:10.1039/d2cp00560c
- Xie, M., Gao, M., Yun, Y., Malmsten, M., Rotello, V. M., Zboril, R., et al. (2023). Antibacterial nanomaterials: mechanisms, impacts on antimicrobial resistance and design principles. *Angew. Chem. Int. Ed.* 62, e202217345. doi:10.1002/anie.202217345
- Yue, Y., Xu, Z., Ma, K., Huo, F., Qin, X., Zhang, K., et al. (2023). HSA shrinkage optimizes the photostability of embedded dyes fundamentally to amplify their efficiency as photothermal materials. *Chin. Chem. Lett.*, 109223. doi:10.1016/j.ccl.2023.109223
- Zeng, X., Shan, C., Sun, M., Ding, D., and Rong, S. (2022). Graphene enhanced α -MnO₂ for photothermal catalytic decomposition of carcinogen formaldehyde. *Chin. Chem. Lett.* 33, 4771–4775. doi:10.1016/j.ccl.2021.12.085
- Zhang, C., He, W., Liu, C., Jiao, D., and Liu, Z. (2021). Cutting-edge advancements of nanomaterials for medi-translatable noninvasive theranostic modalities. *VIEW* 2, 20200144. doi:10.1002/viw.20200144
- Zhao, J., Yu, D., Chen, J., Lin, S., Tang, Y., Fan, C., et al. (2023). Deciphering the high-carbonization-temperature triggered enzymatic activity of wool-derived N, S-co-doped carbon nanosheets. *Chin. Chem. Lett.* 35, 109080. doi:10.1016/j.ccl.2023.109080
- Zhu, Q., Li, P., Huang, Q., Ding, X., Wang, N., Yao, W., et al. (2023). Near-infrared light-activatable melanized paclitaxel nano-self-assemblies for synergistic anti-tumor therapy. *J. Analysis Test.* 7, 204–214. doi:10.1007/s41664-023-00262-2